at the blue end of the spectra, and because the historical spectrum did not include the SiIV line. We also derive from the digitized Palomar Observatory sky surveys (*20*) a differential photometric variation of 0.11 ± 0.45 magnitude. The large error bar may be due to the plate quality and the slight difference in the bandpasses at the two epochs.

For PKS 0424−13 [z = 2.17, M_B = −28.6 (*19*)], the spectrum obtained on 16 February 1990 shows the CIV line to be 25% stronger than on 20 December 1998, whereas Lyα is ~10% stronger in 1990 than in 1998. The line EW ratio CIV/Lyα is thus 14% larger in 1990 than in 1998. In addition, the CIII] line shows little variation in this object. The CIV line variation is thus constrained from both ends of the spectrum, ruling out the possibility that the observed line variation is caused by continuum shape variation in this object.

Both MRC 0238+100 and PKS 0038−019 are lobe-dominant with clear double-lobed radio structures (*22*). The ratios of core to total radio flux density of MRC 0238+100 and PKS 0038−019 at rest frame 5 GHz are 0.098 and 0.067, respectively (*23*). The lobe-dominant radio structure of PKS 0424−13 is implied by its steep radio spectrum (*24*). We do not expect to see the variable blazar continuum at such large implied viewing angles away from the beam. Although some large apparent emission line variations have been reported in core-dominant quasars with large continuum variations [e.g., an EW change of 68% in CIV and 82% in CIII] for 3C446 (*18*)], no large line ratio variations comparable to the cases of MRC 0238+100 and UM 556 have been reported so far, except for the low-luminosity AGN NGC 5548 [e.g., (*25*), where a HeII (468.6 nm) flare was interpreted as an accretion event]. We also note that because 90% of quasars are radio-quiet, some of them have inevitably been observed more than once, yet no large line ratio variations have been published (*26*).

Our observations offer support for the unified scheme for radio-loud quasars. The emission line variations provide the most direct evidence for the existence of violent blazar outbursts in every radio-loud quasar. Similar ideas can be applied to other jet-disk systems such as gamma-ray bursts and protostars. In addition, the disk-wind model for the broad line–emitting clouds, with the winds blowing off the accretion disk by radiation pressure (*27*), is challenged because it does not include any gas in the polar regions. Another widely adopted model, the stellar atmosphere model for the BELR (*28*), has been challenged by emission line profile studies (*29*). Hence, other explanations for the origin of BELR gas may be needed. Finally, our results suggest that radio-loud quasars should be excluded when studying cosmology via the Baldwin effect [the inverse relation between EW (CIV) and continuum luminosity (*30*)]. Reducing the scatter in this relation is critical for using quasars as luminosity indicators (*31*), whereas radio-loud quasars introduce extra scatter as a result of their hidden blazar activity.

References and Notes

1. J. G. Hills, *Nature* **254**, 295 (1975).
2. G. A. Shields, *Nature* **272**, 706 (1978).
3. A. Laor, *Astrophys. J.* **543**, L111 (2000).
4. R. D. Blandford, R. L. Znajek, *Mon. Not. R. Astron. Soc.* **179**, 433 (1977).
5. R. Antonucci, *Annu. Rev. Astron. Astrophys.* **31**, 473 (1993).
6. C. M. Urry, P. Padovani, *Pub. Astron. Soc. Pac.* **107**, 803 (1995).
7. F. Ma, B. J. Wills, *Astrophys. J.* **504**, L65 (1998).
8. J. R. Webb *et al.*, *Astron. J.* **100**, 1452 (1990).
9. S. Kaspi, H. Netzer, *Astrophys. J.* **524**, 71 (1999).
10. D. Maoz, P. S. Smith, B. T. Jannuzi, S. Kaspi, H. Netzer, *Astrophys. J.* **421**, 34 (1994).
11. S. Kaspi *et al.*, *Astrophys. J.* **533**, 631 (2000).
12. M. R. Corbin, P. S. Smith, *Astrophys. J.* **532**, 136 (2000).
13. I. M. Hook, R. G. McMahon, B. J. Boyle, M. J. Irwin, *Mon. Not. R. Astron. Soc.* **268**, 305 (1994).
14. S. Cristiani *et al.*, *Astron. Astrophys.* **306**, 395 (1996).
15. M. R. S. Hawkins, *Astron. Astrophys.* **143**, 465 (2000).
16. J. C. Shields, G. J. Ferland, B. M. Peterson, *Astrophys. J.* **441**, 507 (1995).
17. P. D. Barthel, D. R. Tytler, B. Thomson, *Astron. Astrophys. Suppl. Ser.* **82**, 339 (1990).
18. E. Pérez, M. V. Penston, M. Moles, *Mon. Not. R. Astron. Soc.* **239**, 55 (1989).
19. M. P. Véron-Cetty, P. Véron, *ESO Sci. Rep. 17* (1996).
20. I. N. Reid *et al.*, *Pub. Astron. Soc. Pac.* **103**, 661 (1991).
21. S. Mitton, C. Hazard, J. A. J. Whelan, *Mon. Not. R. Astron. Soc.* **179**, 569 (1977).
22. P. D. Barthel, G. K. Miley, R. T. Schilizzi, C. J. Lonsdale, *Astron. Astrophys. Suppl. Ser.* **73**, 515 (1988).
23. K. Nilsson, *Astron. Astrophys. Suppl. Ser.* **132**, 31 (1998).
24. P. D. Barthel, G. K. Miley, *Nature* **333**, 319 (1988).
25. B. M. Peterson, G. J. Ferland, *Nature* **324**, 345 (1986).
26. T. Small, W. L. W. Sargent, and C. C. Steidel [*Astron. J.* **114**, 2254 (1997)] reported a large apparent CIV emission line variation in the radio-quiet quasar Q 0946+3009 from 1990 to 1992. However, in their analysis of the spectra, rather subjectively chosen continua at the two epochs were used and were subtracted from the original data. By reanalyzing their original data using our method, we found no CIV emission line variation [F. Ma, thesis, University of Texas at Austin (2000)]. Undulations in the division spectrum are seen and are probably the result of calibration errors.
27. N. Murray, J. Chiang, S. A. Grossman, G. M. Voit, *Astrophys. J.* **451**, 498 (1995).
28. T. Alexander, H. Netzer, *Mon. Not. R. Astron. Soc.* **270**, 781 (1994).
29. N. Arav, T. A. Barlow, A. Laor, W. L. W. Sargent, R. D. Blandford, *Mon. Not. R. Astron. Soc.* **297**, 990 (1998).
30. J. A. Baldwin, *Astrophys. J.* **214**, 679 (1977).
31. J. Baldwin, in *Quasars and Cosmology*, G. Ferland, J. Baldwin, Eds. (Astronomical Society of the Pacific, San Francisco, 1999), p. 475.

32. We thank J. Baldwin, P. Barthel, P. Francis, T. Small, M. Vestergaard, and J. Yuan for making their data available in digital form; G. Shields for helpful discussions; D. Wills for help with the manuscript; and D. Doss and M. Prado for their supporting work at McDonald Observatory. This work makes use of the Space Telescope Science Institute (STScI) Digitized Sky Survey and the NASA/IPAC Extragalactic Database (NED).

5 March 2001; accepted 7 May 2001

Observation of Magnetic Hysteresis at the Nanometer Scale by Spin-Polarized Scanning Tunneling Spectroscopy

O. Pietzsch,* A. Kubetzka, M. Bode, R. Wiesendanger

Using spin-polarized scanning tunneling microscopy in an external magnetic field, we have observed magnetic hysteresis on a nanometer scale in an ultrathin ferromagnetic film. An array of iron nanowires, being two atomic layers thick, was grown on a stepped tungsten (110) substrate. The microscopic sources of hysteresis in this system—domain wall motion, domain creation, and annihilation—were observed with nanometer spatial resolution. A residual domain 6.5 nanometers by 5 nanometers in size has been found which is inherently stable in saturation fields. Its stability is the consequence of a 360° spin rotation. With magnetic memory bit sizes approaching the superparamagnetic limit with sub–10 nanometer characteristic lengths, the understanding of the basic physical phenomena at this scale is of fundamental importance.

The investigation of magnetic nanostructures has been hampered by the lack of magnetic imaging techniques with an adequate spatial resolution [for an overview on the relevance of such structures see, e.g., (*1*)]. A scanning tunneling microscope is expected to be the ultimate microscopic magnetic investigation tool if the tip itself is a source of spin-polarized electrons (*2*). First reports on spin-polarized scanning tunneling microscopy (SP-STM) 10 years ago (*3, 4*) have shown that the use of magnetic probe tips provides

Institute of Applied Physics and Microstructure Research Center, University of Hamburg, Jungiusstrasse 11, D-20355 Hamburg, Germany.

*To whom correspondence should be addressed. E-mail: pietzsch@physnet.uni-hamburg.de

an appropriate approach in achieving this goal. More recently, the in-plane magnetic domain structure of nanometer-scale Gd islands and also perpendicularly magnetized nanostructures have been resolved utilizing tunneling tips with a ferromagnetic thin-film coating in conjunction with a spectroscopic mode of STM operation (*5, 6*). Moreover, SP-STM has recently provided first atomic-resolution real-space images of an antiferromagnetically ordered Mn monolayer (*7*) demonstrating that STM-based magnetic imaging has become a mature technique. Nanometer-scale magnetic imaging is particularly challenging if a strong external magnetic field is to be applied to the system under study, a condition being, in general, prohibitive for microscopy techniques relying on a yield of secondary electrons. Acquisition of hysteresis curves of thin films remained mainly the realm of techniques using polarized photons as a probe such as magneto-optical Kerr effect measurements, which, even if applied as a microscopy method, suffer from an appropriate spatial resolution owing to the limit of optical wavelengths. It is clear that the signal obtained is spatially averaged over a considerable fraction of the surface. In magnetic transmission x-ray microscopy strong variable magnetic fields can be applied to the sample, and a resolution better than 100 nm has been achieved (*8*). A comparable resolution has been obtained in both Fresnel and Foucault microscopy in external fields up to ~1 T (*9*). Also, arrays of magnetic elements as small as 200 nm by 40 nm have been observed at different stages of a magnetization cycle using various modes of Lorentz microscopy (*10*). Ballistic electron magnetic microscopy (BEMM) has recently been introduced as a new method for domain observation (*11–13*). A nonmagnetic STM tip is used to locally inject a current into a trilayer consisting of two thin ferromagnetic films separated by a non-magnetic spacer layer deposited on a semiconductor substrate. As ballistic electron transport into the semiconductor is enhanced (reduced) for regions of parallel (antiparallel) magnetization alignment of the ferromagnetic films BEMM images display maps of the relative orientation of the magnetic films as a function of the tip position. This technique has been used to study the magnetization reversal in nanostructures at ~50 nm resolution.

We report an SP-STM study of the effect of an external magnetic field on the magnetic domain structure of a self-organized array of Fe nanowires grown pseudomorphically on a stepped W(110) single crystal. A similar system has been investigated by magneto-optical Kerr effect measurements (*14*), i.e. by a spatially averaging technique which is unable to resolve the underlying nanometer-sized domain structure. We present a detailed study of the changes the domain structure undergoes in an applied field. The images obtained allow direct extraction of a hysteresis curve based on information acquired at the nanometer scale. Moreover, we imaged the processes behind hysteresis, i.e. domain wall motion, domain creation and annihilation. A stable residual domain is found which is, due to its small size, inaccessible to imaging methods other than SP-STM.

The experiments were performed in an ultrahigh vacuum STM system especially designed for magnetic imaging, equipped with a 2.5-T superconducting magnet (*15*). Details of the preparation and the structural and magnetic properties of sample and ferromagnetic STM tip are described elsewhere (*6*). In short, an Fe film with a nominal thickness of 1.65 pseudomorphic atomic layers was deposited onto a stepped W(110) single crystal held at 450 ± 50 K. This preparation leads to step-flow growth resulting in a system of stripes of alternating monolayer (ML) and double layer (DL) thickness which extends along the W terrace steps (*14*). Although the ML stripes are magnetized in the sample plane with the easy axis along [1$\bar{1}$0], the DL stripes exhibit a perpendicular easy axis with an antiparallel coupling of adjacent DL stripes resulting from dipolar interaction (*6, 14, 16*). The structural periodicity of the DL stripes is determined by the miscut of the underlying W substrate and amounts to 9 nm on average. At the chosen coverage, the DL stripes have an average width of W = 5.8 nm and a variation of local widths between 10 nm and less than 2 nm. We used a W STM tip coated with 8 ± 1 ML of Gd. The tip is then magnetized along its axis, i.e. perpendicular to the sample plane. In all measurements, tip and sample had a temperature of T = 14.5 ± 1 K.

Evolution of the DL magnetic domain structure as a function of a variable magnetic field applied perpendicular to the sample plane is shown in 12 frames selected from a series of 24 images (*17*). The scan range is 200 nm by 200 nm. The signal providing the contrast is the differential tunneling conductance dI/dU which is acquired by a lock-in technique simultaneously to the topographic image [not shown here; for details of the imaging process, see (*5, 6*)]. At the chosen bias voltage of +700 mV, the ML areas exhibit the lowest differential conductance and appear black in all the images. In DL stripes a two-stage contrast is observed, the latter being of magnetic origin. Using a ferromagnetic probe tip, the spin valve effect can be exploited as a contrast mechanism: the differential conductance will be different at

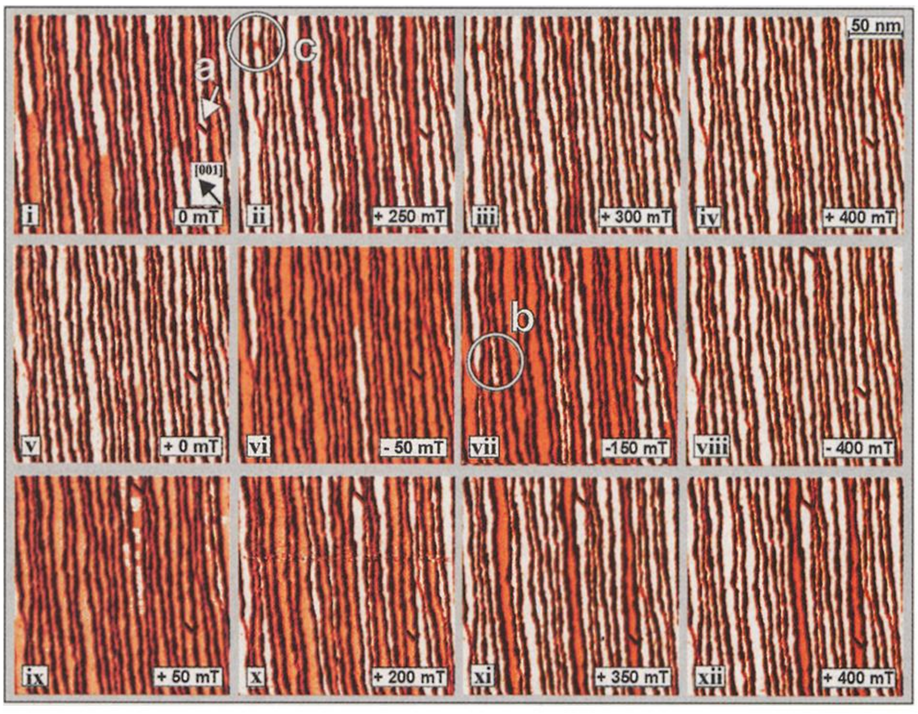

Fig. 1. Twelve images selected from a series of 24 taken at field values as indicated (*17*). Scan range is 200 nm by 200 nm. Because of the growth conditions (see text), a system of alternating ML and DL Fe stripes emerges on the W terraces. When measured with a ferromagnetic probe tip with perpendicular anisotropy, DL stripes show a two-stage contrast in the conductance map. It arises from the out-of-plane magnetization of DL stripes, being either parallel or antiparallel to the tip magnetization (spin valve effect). As a guide to the eyes, a dislocation line (a) is marked. Dark domains progressively vanish as positive field increases, and at saturation, only bright domains remain. High remanence is observed. A small negative field of –50 mT is sufficient to switch the tip magnetization whereas the sample stays almost unaffected. A contrast reversal results [compare (v) and (vi)]. At negative saturation, all stripes are once again bright (viii). Circles (b) and (c) refer to the enlarged views given in Figs. 3 and 4. Tunneling parameters: I = 0.5 nA, U = +700 mV.

sample locations having a magnetization parallel to the tip magnetization as compared to locations being magnetized antiparallel. Thus, given an appropriate anisotropy of the tip, a dI/dU-map provides an image of the magnetic domain structure of the sample.

In the magnetic virgin state of the sample [Fig. 1(i)], the antiparallel order of the DL areas shows up as alternating white and red stripes (in the following, the DL contrasts will be referred to as bright and dark). Within the frame, 15 domain boundaries can be seen, and a certain tendency to form spatial correlations of domain walls among neighboring stripes in a checkerboard manner is found. The widths of the walls confirm the previously reported result of 6 ± 1 nm (*6*). As the overall distribution of bright and dark DL areas is balanced, the sample is macroscopically demagnetized.

Panels (ii) to (xii) show the development of the domains as a function of the external magnetic field. With increasing positive field bright areas grow at the expense of dark areas until, at +400 mT, almost all dark DL areas have vanished indicating saturation [Fig. 1(iv)]. So far, we can identify bright areas as being magnetized parallel to the external field, i.e. up (↑), whereas the dark domains are magnetized down (↓). High remanence is observed [Fig. 1(v)].

Taking the step from remanence to –50 mT [Fig. 1, (v) and (vi)], a change takes place in the distribution of bright and dark. The contrast of all DL stripes is reversed. This is explained by a switching of the tip's magnetization by the external field from (↑) to (↓) while the sample remains almost unaffected. As a consequence, at (↑) domains the tip-sample configuration is changed from (↑↑) to (↓↑), and the opposite happens for (↓) domains where (↑↓) is changed to (↓↓).

A further field increase in $-z$ direction leads again to a growth of bright DL domains until, at −400 mT, saturation in the negative direction is reached, again with no dark domains left [Fig. 1(viii)]. At +50 mT, the tip has switched again [Fig. 1(ix)], symmetrical to the previous switching event, and the effect on the images is analogous. This observation allows an estimation of the coercive field for the Gd tip, $\mu_0 H_C^{\mathrm{tip}} \leq 50$ mT.

By evaluating the bright DL stripe length percentage we obtain the butterfly hysteresis curve displayed in Fig. 2A. The shape of this curve results from the fact that two ferromagnetic electrodes are involved, namely tip and sample. Taking the effect of tip switching into account pure sample properties can easily be separated. They are represented by the second hysteresis curve (Fig. 2B) which displays the percentage of (↑) domains as a function of the applied field. A remanence-to-saturation ratio $M_R/M_S \approx 0.98$ is observed. The sample coercivity is $\mu_0 H_C^{\mathrm{sample}} \approx 200 \pm 50$ mT. The corresponding domain structure is shown in Fig. 1(x). Comparing this frame to the initial demagnetized state [Fig. 1(i)], we observe that the detailed magnetic order of the stripes has changed significantly. No domain wall can be found at its initial location. This is not surprising, because the existence of a hysteresis is already a consequence of the irreversibility of the remagnetization process. The initial contrast pattern alternating from one stripe to the next is replaced by an occurrence of bunches of two, three, or even four stripes of the same magnetization next to bundles of stripes of opposite magnetization. The dipolar order has coarsened significantly, attributed to the different history of these demagnetized states. The initial order was formed when the sample was cooled down from its growth temperature to 14.5 K. At the DL Curie temperature $T_C^{\mathrm{DL}} = 300$ K (*18*), the thermal energy is of a magnitude comparable to that of the magnetization-related energy contributions. This supports the formation of a fine-sized equilibrium order such that the stray field energy is minimized. This effect of thermal energy is greatly reduced at low temperatures. The virgin state emerged from a transition from the paramagnetic phase with no magnetic order, whereas coercivity was preceded by saturation with all domains perfectly aligned, i.e., maximum magnetic order.

The general shape of the hysteresis loop of Fig. 2B is not a simple square loop but shows a slope. It is clear that the magnetic reorientation does not take place in a single jump from one saturated state to the opposite one but progresses successively. Except for the weak spatial correlations of domain walls mentioned earlier caused by dipolar interaction, the DL stripes are found to be effectively decoupled even by ML stripes as narrow as ≈1.5 nm. Every single stripe is remagnetized individually. Two mechanisms of remagnetization are observed, domain creation and domain wall motion. Wall motion is restricted to the direction along the stripe. Both mechanisms are illustrated in Fig. 3A, taken at the location marked (b) in Fig. 1. Two new domains (a) and (b) are created. Because the spins have to rotate continuously at both domain ends, the sense of rotation within

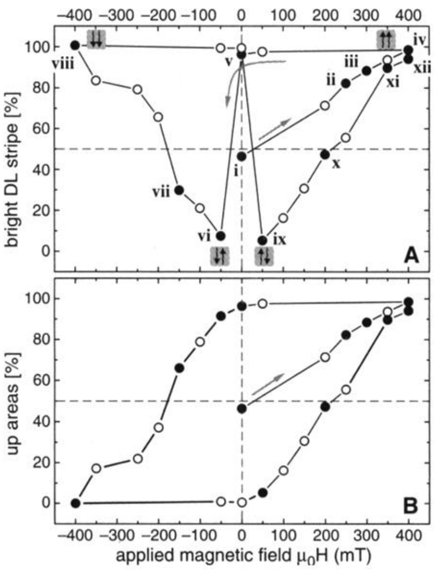

Fig. 2. Hysteresis curves obtained from the distribution of bright domains (**A**) and stripes with $+z$ magnetization (↑) (**B**). The butterfly curve in (A) shows properties of the complete tunneling junction consisting of two ferromagnetic electrodes, whereas the curve in (B) displays only sample properties. Arrow symbols in (A) indicate the relative alignment of tip and sample magnetization. Roman numbers at solid circles correspond to the images shown in Fig. 1.

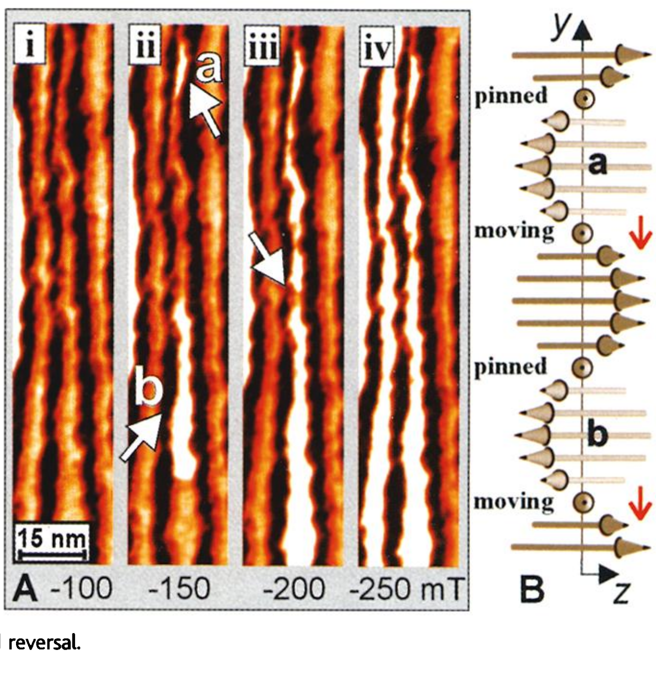

Fig. 3. (**A**) Creation and annihilation of domains. Two new bright domains, marked (a) and (b), are being created, bounded by Bloch walls. The lower wall of (a) moves toward (b), and the trapped dark area shrinks. The last dark portion is marked by an arrow in (iii), immediately before it gets annihilated. (**B**) Sketch of the magnetization reorientation process roughly at the stage of panel (ii) (side view, not to scale). Arrows indicate the magnetization direction. Note the vector orientation at the wall centers, all pointing into the same direction. The new domains will again be annihilated on field reversal.

the two Bloch walls bounding a new domain must be opposite, namely +180° and –180° (Fig. 3B). With increasing field, the lower wall of domain (a) moves toward domain (b). Finally, (a) and (b) merge, which is equivalent to an annihilation of the dark domain trapped between them. In panel (iii), the last dark portion, marked by an arrow, is visible just before it vanishes. From the viewpoint of the dark domain, its bounding walls get unwound. On field reversal, the new bright domain will also be annihilated because the same arguments apply.

In Fig. 1, (ii) through (iv), a dark spot marked (c) is present which is a relict of the dark domain visible in Fig. 1(i). This spot retains its size and position regardless of the increasing field and serves as a nucleation center for an extended dark domain in this particular wire at decreasing field [Fig. 1(v)]. An enlarged view of this small domain, taken at +400 mT, is presented in Fig. 4A. Its surprising stability can be understood in the following way: Due to the increasing field a dark domain has shrunken. Its two domain walls approach each other and end up in direct contact. However, the domain can only be annihilated if the sense of rotation inside its bounding walls is opposite. This was the case in the previously discussed example. If, on the other hand, both walls exhibit the same sense of rotation the result is a total spin rotation of 360° which is inherently stable in an external field. To overcome such a configuration a breakdown process is required, with external fields equal to the exchange field B_{ex} which can be roughly estimated from considering $\mu_B B_{ex} \approx k_B T_C$ (*19*), with μ_B as the Bohr magneton and k_B as Boltzmann's constant. Taking $2.2\mu_B$ for Fe yields $B_{ex} \approx 200$ T, a value not accessible by laboratory magnets. The actual value remains to be investigated and may be considerably smaller due to the reduced number of nearest-neighbor atoms in a film as thin as two ML (six instead of eight in the bulk), with this number even more reduced to three at the step edges, but B_{ex} may still be large. In this picture the smallest possible stable domain exhibiting a magnetization direction opposed to the external field is the result of two 180° walls forced together in a winding process by the external field. We have fitted two tan*h* standard wall profiles to the d*I*/d*U*-signal assuming a 360° rotation (see the red line in Fig. 4B), thereby determining the length of the residual domain to $L = 6.5 \pm 0.5$ nm; a 180° spin rotation thus takes place over 42 ± 4 atomic rows. Due to their small size, the presence of residual domains will not be noticeable in conventional, spatially averaging measurements of a hysteresis loop. However, we can expect the question of their existence to be crucial for the remagnetization process, opening two different paths: (i) a first degree of saturation is attained when only residual domains are left in the sample. They will act as seeds for a magnetization reversal. (ii) If all residual domains can get eliminated, which requires much higher fields, then reversed domains must be nucleated as a first step of the magnetization reversal.

The requirement of a 360° spin rotation implies that, at the wall centers, the magnetization vectors lie in the sample plane pointing in opposite directions. This can be made visible by using a ferromagnetic tip with in-plane anisotropy being sensitive to the domain walls rather than to the domains (*20*). Figure 4C was imaged with a W tip coated with 5 ± 1 ML Fe (*5*). It shows a similarly prepared sample in its magnetic virgin state exhibiting a strictly alternating order of bright and dark domain walls. So far, we never observed two walls of the same type next to each other in a virgin sample. Any pair of walls within a single stripe may thus form a residual domain regardless of the polarity of the saturated state. The image suggests that a sufficient number of nuclei will be available for a magnetization reversal.

In conclusion, SP-STM–based magnetic imaging allows for a study of magnetic nanostructures in strong magnetic fields at a scale that is characterized by the magnetic exchange length. The method may contribute to an improved understanding of the basic physical phenomena relating magnetism to surface properties like structural and chemical roughness, or to the presence of single impurity atoms and defects.

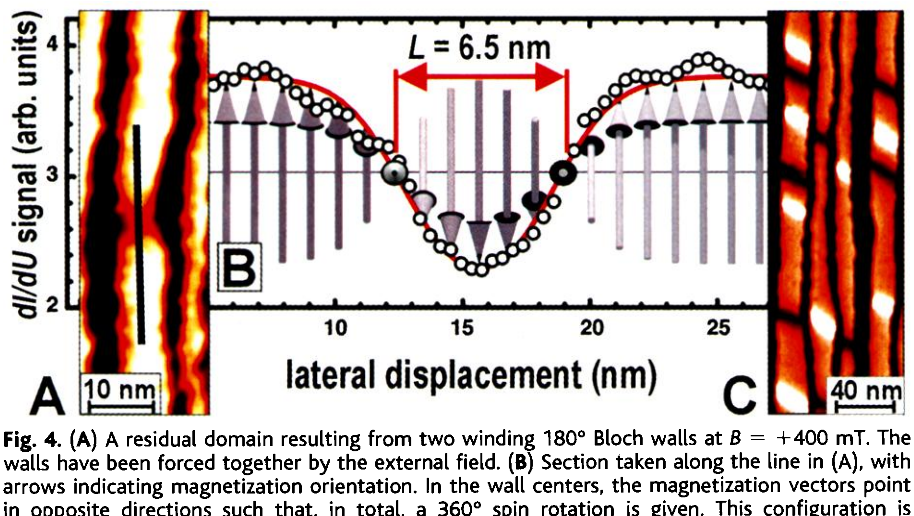

Fig. 4. **(A)** A residual domain resulting from two winding 180° Bloch walls at $B = +400$ mT. The walls have been forced together by the external field. **(B)** Section taken along the line in (A), with arrows indicating magnetization orientation. In the wall centers, the magnetization vectors point in opposite directions such that, in total, a 360° spin rotation is given. This configuration is inherently stable in an applied external field and thus constitutes the smallest possible domain with a magnetization opposite to the field. On field reversal, such residual domains provide nuclei for the remagnetization. **(C)** A virgin sample as imaged by a Fe-coated tip with in-plane sensitivity. High contrast is then found in domain walls. The walls show an alternating orientation along each stripe. For any pair of walls within a stripe, a 360° spin rotation is given.

References and Notes

1. F. J. Himpsel, J. E. Ortega, G. J. Mankey, R. F. Willis, *Adv. Phys.* **47**, 511 (1998).
2. D. T. Pierce, *Phys. Scripta* **38**, 291 (1988).
3. R. Wiesendanger, H.-J. Güntherodt, G. Güntherodt, R. J. Gambino, R. Ruf, *Phys. Rev. Lett.* **65**, 247 (1990).
4. R. Wiesendanger *et al.*, *Science* **255**, 583 (1992).
5. M. Bode, M. Getzlaff, R. Wiesendanger, *Phys. Rev. Lett.* **81**, 4256 (1998).
6. O. Pietzsch, A. Kubetzka, M. Bode, R. Wiesendanger, *Phys. Rev. Lett.* **84**, 5212 (2000).
7. S. Heinze *et al.*, *Science* **288**, 1805 (2000).
8. T. Eimüller *et al.*, *J. Appl. Phys.* **87**, 6478 (2000).
9. V. V. Volkov, Y. Zhu, *J. Magn. Magn. Mater.* **214**, 204 (2000).
10. K. J. Kirk, J. N. Chapman, S. McVitie, P. R. Aitchison, C. D. W. Wilkinson, *Appl. Phys. Lett.* **75**, 3683 (1999).
11. W. H. Rippard, R. H. Buhrman, *Appl. Phys. Lett.* **75**, 1001 (1999).
12. ———, *Phys. Rev. Lett.* **84**, 971 (2000).
13. W. H. Rippard *et al.*, *Appl. Phys. Lett.* **77**, 1357 (2000).
14. J. Hauschild, U. Gradmann, H. J. Elmers, *Appl. Phys. Lett.* **72**, 3211 (1998).
15. O. Pietzsch, A. Kubetzka, D. Haude, M. Bode, R. Wiesendanger, *Rev. Sci. Instrum.* **71**, 424 (2000).
16. H. J. Elmers, J. Hauschild, U. Gradmann, *Phys. Rev. B* **59**, 3688 (1999).
17. The complete set of all 24 images is available at www.sciencemag.org/cgi/content/full/292/5524/2053/DC1.
18. H. J. Elmers, in *Magnetische Schichtsysteme in Forschung und Anwendung* (Institut für Festkörperforschung der Forschungszentrum Jülich GmbH, Jülich, Germany, 1999), p. B1.41.
19. W. Nolting, *Quantentheorie des Magnetismus* (Teubner, Stuttgart, Germany, 1986), vol. 1, p. 229.
20. Direct observation of pure Bloch walls is particularly challenging and is restricted to ultrathin films with perpendicular anisotropy, where the film thickness is much smaller than the magnetic exchange length, $t \ll \sqrt{A/K}$, with *A* and *K* denoting the constants of exchange stiffness and anisotropy, respectively. In thicker films, a Bloch wall will be capped at the surface by a Néel type wall due to large dipolar fields across the wall giving rise to a twisting of the wall magnetization in the near-surface region (*21*, *22*). Only in very thin films is this effect suppressed by the exchange stiffness energy.
21. J. C. Slonczewski, *J. Appl. Phys.* **44**, 1759 (1973).
22. E. Schlömann, *J. Appl. Phys.* **44**, 1873 (1973).

23. Financial support from the Deutsche Forschungsgemeinschaft (grant Wi 1277/9), from the German Israeli Foundation for Scientific Research and Development (GIF) (grant I-550-184.14/97), and from the Bundesministerium für Bildung, Wissenschaft, Forschung und Technologie (BMBF) (grant 13N7647) is gratefully acknowledged.

8 March 2001; accepted 14 May 2001